ORNL/TM-2023/3200

Advanced Manufacturing Workflows for Tokamak Internal Components

Andrzej Nycz
Yukinori Yamamoto
Luke Meyer
Chris Masuo
William Carter
Peter Wang
Alex Walters
Deepthi Tammana (CFS)
Shiyun Ruan (CFS)
Cody Dennett (CFS)

CRADA Final Report
NFE-21-08652

December 2023

OAK RIDGE National Laboratory

ORNL IS MANAGED BY UT-BATTELLE LLC FOR THE US DEPARTMENT OF ENERGY

ORNL/TM-2023/3200

Manufacturing Science Division

ADVANCED MANUFACTURING WORKFLOWS FOR TOKAMAK INTERNAL COMPONENTS

Author(s)

Andrzej Nycz
Yukinori Yamamoto
Luke Meyer
Chris Masuo
William Carter
Peter Wang
Alex Walters
Deepthi Tammana (CFS)
Shiyun Ruan (CFS)
Cody Dennett (CFS)

December 2023

Prepared by
OAK RIDGE NATIONAL LABORATORY
Oak Ridge, TN 37831
managed by
UT-BATTELLE LLC
for the
US DEPARTMENT OF ENERGY
under contract DE-AC05-00OR22725

CONTENTS

ABSTRACT

The project aim was to create a new advanced manufacturing workflow for the design and creation of an internal component in a fusion device, enabling a low-cost, rapid design and fabrication cycle. As a result, two demonstration components were manufactured, and mechanical properties for two feedstock materials were tested in the context of fusion device conditions. This work shows a technological scoping toward future manufacturing of complex components in topologies relevant to magnetic fusion devices via additive manufacturing.

1. INTRODUCTION

1.1 PURPOSE AND BACKGROUND

This is a report under CRADA (NFE-21-08652) between Oak Ridge National Laboratory (Contractor) with Commonwealth Fusion Systems under the INFUSE program.

The objective of this project was to design an advanced manufacturing workflow for the design and manufacture of an internal component in a fusion device, enabling a low-cost, rapid design and fabrication cycle consistent with rapid innovation.

Participant is currently designing a commercial fusion device called ARC, which uses a key innovation—high-field high temperature superconducting (HTS) magnets. These allow for reduced plant size and cost. In addition, they allow for resistive, demountable superconducting joints that give ready access to interior components.

To deal with high levels of neutron radiation, heat flux, and corrosion from the molten salt blanket, the ARC vacuum vessel (which includes the first wall and divertor), will be designed to be replaced at a high frequency (every few years) in ARC operation. When combined with demountable superconducting joints, this modularity will allow the removal and replacement of intact, single components in a commercial tokamak. This will therefore allow each integrated vessel to be fully constructed, tested outside the fusion device, and then inserted or replaced as needed, eliminating the need for in-situ assembly.

The ability to replace modular internal components inside a tokamak could substantially decrease the cost of fusion energy by significantly reducing materials challenges and effectively lengthening the lifespan of the overall fusion device. However, the development of demountable superconducting joints is necessary but not sufficient to realize these benefits. An additional, critical need that must be addressed to realize these benefits is the ability to rapidly and inexpensively fabricate the replacement components.

This fabrication method must also be able to scale, not only in the size of components that can be created (torii with major radius ~4m and minor radius ~1m) but also in the widespread adoption of the method to support a fast-growing fusion industry.

In addition, early fusion energy devices will have a learning curve, and there will likely be design changes to internal components. This may require expensive re-tooling unless an adaptable/reconfigurable fabrication method exists. Internal components of fusion energy devices are likely to use novel materials like composites, graded materials, and uniquely joined materials. This is because of the unique and extreme environment including high heat flux, neutron radiation, corrosion from molten salts, and high mechanical stresses. Novel material candidates include tungsten alloys, carbon materials, and oxide dispersion-strengthened (ODS) and reduced activation ferritic-martensitic (RAFM) steels. Fabrication methods for these are not generally known, and the material set has highly variable coefficients of thermal expansion, making joining difficult.

Thus, to support the accelerated development of commercial fusion energy, it is a critical need to have fabrication methods which can support rapid turnaround of design changes and the use of novel materials. Additive manufacturing (AM) is a potential solution to the above challenges and opens the rapid, low-cost fabrication of large components with novel materials.

Contractor is a leader in manufacturing research with expertise in advanced materials, controls and analysis, modeling and advanced characterization, and systems development. Contractor is well positioned to successfully complete this collaboration project and is focused on developing the systems, processes, sensors and controls needed to reinvigorate the US industrial base and bolster national security.

1.2 SCOPE OF WORK

The overall objective was to design a workflow for the design and manufacture of an AM internal component in a fusion device. This workflow was tested and driven by the production of an actual subscale object of an ARC vacuum vessel.

The overall workflow consisted of the following steps: component selection for AM, material selection, printability test, manufacturing of test coupons, verification of material properties, redesign of the parts for AM and near net shape printing, printing of the critical subsections of the component, modification of the deposition process (if necessary) and final production.

At Participant's facilities, optimization engineers worked with plasma and fusion materials experts to select a component benefitting from AM. Based on the component role two feedstock materials were selected to verify their printability and mechanical properties: 316LMn (ER316LMn wire stock) stainless steel and Nitronic 50 (ER209 wire stock).

As a result of this workflow, two different components were manufactured: a magnet support leg and toroidal vessel segment. The first component was manufactured to test the manufacturing of near net shape geometry with a standard material while the second used 316LMn to evaluate a complex manufacturing process described in the following sections.
Wire-arc additive technology was selected and used in this work due to its relative low cost, existing and available feedstock, ability to crate large parts, scalability, and overall robustness [1]

2. WIRE ARC MANUFACTURING

In the first step, a section of a reactor support leg was manufactured to test the viability of additively manufacturing near net shape geometries for fusion reactors. 316LMn stainless steel was selected as suitable feedstock material.

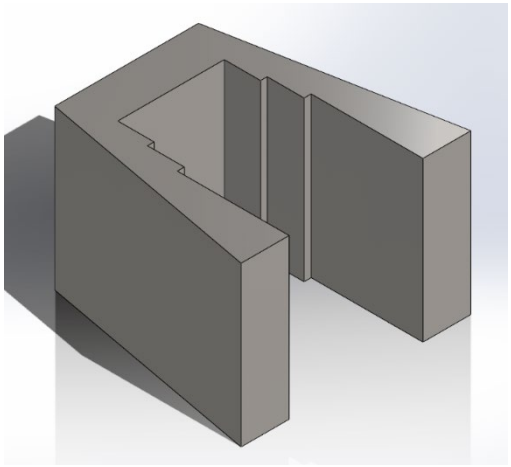

Figure 1 Model of the support leg - defeatured.

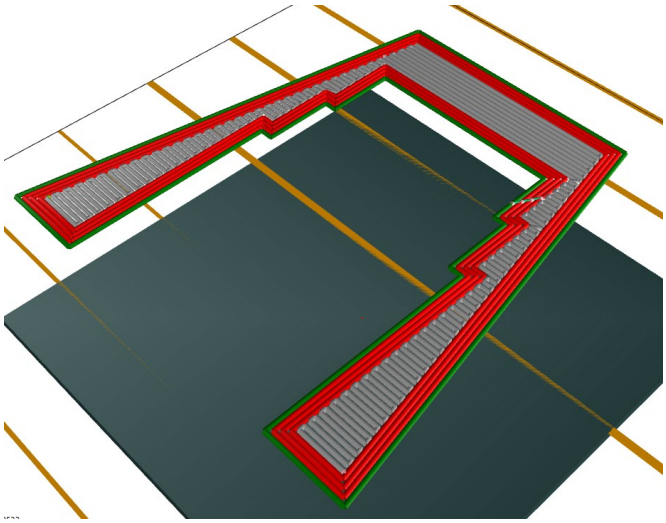

Figure 2. Toolpath visualization

This geometry was selected for printing since this type of geometry (U-shape) would typically require a large amount of machining when manufactured conventionally and result in a large amount of waste. By printing a near-net shape version, the machining time and waste was significantly reduced. It was estimated that ~600lb of material was saved or roughly 60%. The section (Figure 1) was optimized for printing by removing small, hard to print features to decrease the build complexity and adding 5mm overbuild to ensure that the final part was contained within the printed part. This approach allows for high print speed while the fine features can be obtained in the final machining step. The printing toolpath (Figure 2) was designed to create a smooth machining surface (seen by the conformal green and red print path lines) and fast deposition infill (gray internal area). After printing subsections, the final part was manufactured (Figure 3) and delivered to the Participant.

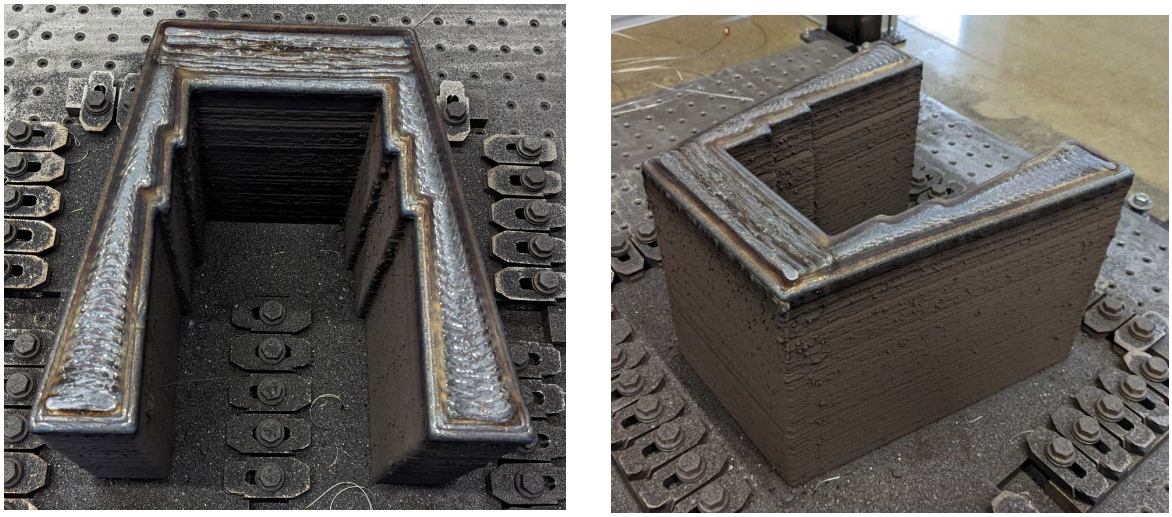

Figure 3. Manufactured near net shape support leg.

3. MATERIALS

3.1 MATERIALS TO BE EVALUATED

Two candidate austenitic stainless steels, 316LMn and Nitronic-50, were selected for evaluation. High manganese addition combining with nitrogen solution in both steels stabilizes the austenite matrix (FCC-Fe) relative to ferrite phase (BCC-Fe), even in a cryogenic atmosphere, which is strongly beneficial for avoiding low-temperature embrittlement observed in typical ferritic steels. No phase transformation, such as martensitic transformation from melting point to ambient temperature, leads to minimized distortion and residual stress accumulation attributed to such phase transformation during printing process. In addition, these steel wires are commercially available and easily procured. **Table 1** summarizes the typical alloy composition range of 316LMn and the alloy specification of Nitronic-50.

Table 1. Typical alloy composition range of 316LMn and alloy specification of Nitronic-50

Alloy	Range of alloying elements, wt.% (balance Fe)									Remarks
	C	N	Mn	Si	Cr	Ni	Mo	Nb	V	
316LMn	0.015 – 0.030	0.15 – 0.18	7.0 – 7.5	0.4 – 0.5	20.0 – 20.5	15.5 – 16.0	3.0	-	-	AWS 5.9: ER316LMn (UNS S31682)
Nitronic-50	0.06 max.	0.20 – 0.40	4.00 – 6.00	1.00 max.	20.5 – 23.5	11.5 – 13.5	1.50 – 3.00	0.10 – 0.30	0.10 – 0.30	XM-19 (UNS S 20910)

As-printed walls of 316LMn are shown in **Figure 4**. Two walls with different wall thicknesses, 2-beads (~0.5-inch) and 4-beads (~0.9-inch), were prepared to machine tensile specimens and Charpy impact specimens, respectively. The wall surfaces were smooth and showed no significant difference in the surface characteristics between 2- and 4-beads walls. Non-destructive evaluation (NDE) through x-ray two-dimensional radiography revealed no major internal defects (large cracks or pores). Two walls of Nitronic-50 were also prepared, and the surface and the NDE results were almost identical to those of 316LMn.

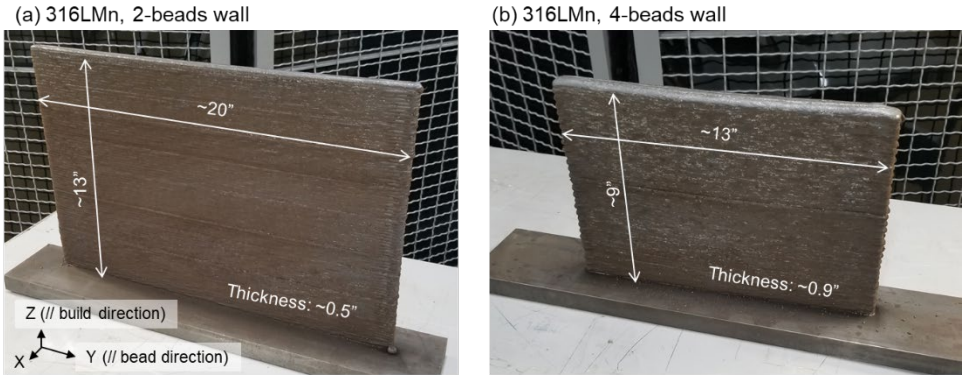

Figure 4. As-printed 316LMn walls with two different wall thicknesses: (a) 2-beads wall (~0.5-inch thickness) and (b) 4-beads wall (~0.9-inch thickness).

3.2 MICROSTRUCTURE CHARACTERIZATION

Microstructure characterization was conducted on the cross-section of the walls. All images shown below were observed from the same direction (// Y-axis or bead direction), and the vertical axis of each image is always parallel to Z-axis (// build direction), unless otherwise noted.

3.2.1 Cross-sectional macrostructure

Macroscopic cross-sectional images of the as-printed 4-beads walls, 316LMn and Nitronic-50, are shown in **Figure 5**. The weld beads consisted of columnar grains were periodically stuck with distinct boundary at the bottom of the beads. There were no physical defects (e.g., cracks) along the columnar grains or the bead boundary. Many columnar grains are connected through the bead boundary, and the length of some of these grains are more than 10 mm. There are no significant differences between the macroscopic characteristics of 316LMn and Nitronic-50.

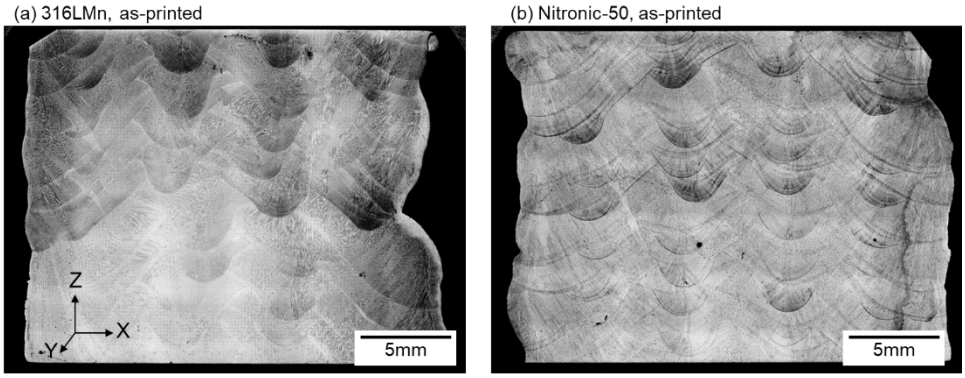

Figure 5. Cross-sectional macroscopic images: (a) 316LMn, 4-beads, and (b) Nitronic-50, 4-beads.

3.2.2 Microstructure

Optical micrographs of the as-printed materials are shown in **Figure 6**. The as-printed 316LMn showed only austenite matrix with dendritic structure observed through a shallow contrast, possibly due to Cr and Mo-enrichment within the dendritic arm spacing. On the other hand, the as-printed Nitronic-50 revealed dark contrast phase at the middle of dendritic arm, corresponding to a residue of primary δ-ferrite phase after an incomplete peritectic reaction of $L + \delta \rightarrow \gamma$.

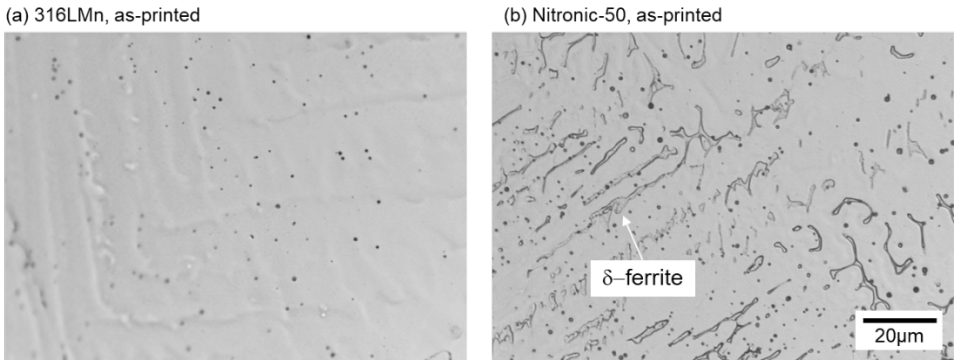

Figure 6. Optical micrographs showing as-printed microstructure: (a) 316LMn, and (b) Nitronic-50.

Since δ-ferrite is known to deteriorate low-temperature mechanical properties due to embrittlement below ductile-brittle transition temperature (DBTT), an additional heat-treatment would be required for Nitronic-50 to eliminate or minimize such δ-ferrite. Based on this consideration, the printed Nitronic-50 was solution-annealed at 1250°C for 1 h (followed by air-cooling) and then subjected to microstructure characterization by scanning electron microscopy (SEM). The SEM-backscattered electron (BSE) images of the as-printed materials and the annealed Nitronic-50 are shown in **Figure 7**. The as-printed 316LMn

was free from δ-ferrite, whereas a lot of δ-ferrite (dark contrast) was observed in the as-printed Nitronic-50, similar to the optical micrographs. After annealing, only a limited amount of δ-ferrite was observed in the "annealed" Nitronic-50. It should be emphasized that a similar amount of δ-ferrite was observed after annealing at 1225 and 1275°C for 1 h, suggesting that a temperature variation within +/-50°C would not be critical for microstructure control.

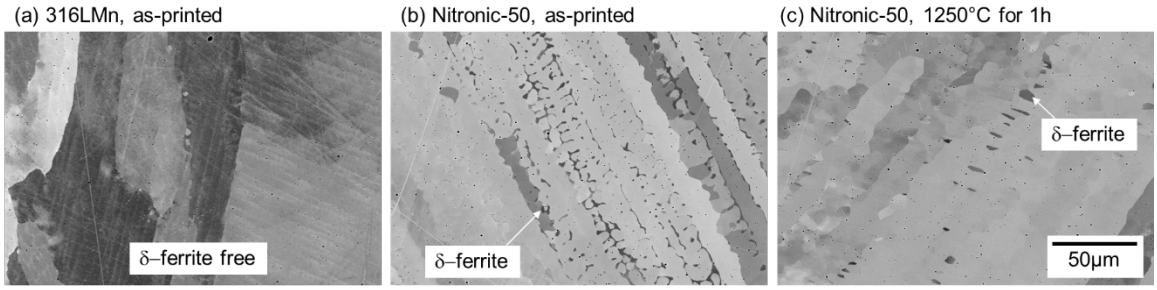

Figure 7. SEM-BSE images showing distribution of primary δ-ferrite phase in the austenite matrix: (a) 316LMn, as-printed, (b) Nitronic-50, as-printed, and (c) Nitronic-50, annealed at 1250°C for 1 h.

3.2.3 Crystallographic orientation analysis

Crystallographic orientation of the as-printed and annealed samples was measured using SEM-Electron Back Scattered Diffraction (EBSD). **Figure 8** represents inverse pole figure (IPF) color maps of the as-printed 316LMn acquired through Orientation Image Mapping (OIM) software, showing the crystallographic orientation of each grain parallel to the build direction (Z-axis, 5a) and to the bead direction (Y-axis, 5b). The results indicated that the as-printed 316LMn was strongly textured with <101> direction parallel to the build direction and <001> direction parallel to the bead direction, resulting in a single crystal-like structure. Similar crystallographic characteristics were observed in the as-printed or annealed Nitronic-50, and it could be the source of anisotropic mechanical properties as described in the next section. Such texture formation was frequently observed in 316L type additively manufactured materials, and the details can be found elsewhere [2].

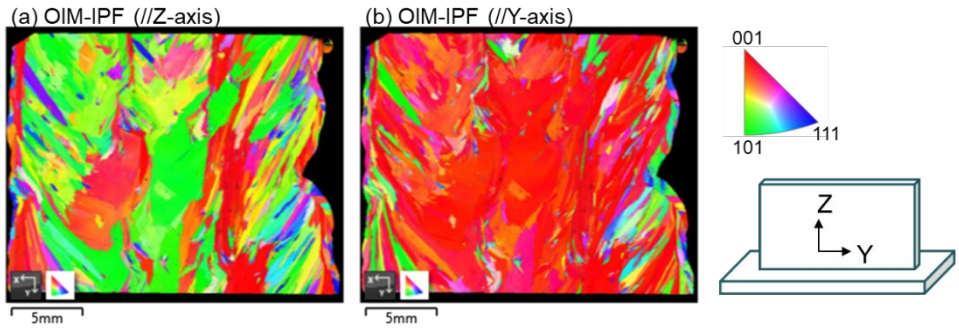

Figure 8. IPF color maps of the as-printed 316LMn acquired through OIM software: (a) orientation parallel to the build direction (Z-axis) and (b) to the bead direction (Y-axis).

3.3 MECHANICAL PROPERTIES

3.3.1 Tensile properties

Tensile properties of the materials at room temperature (RT) and -196°C (77K) are summarized in **Figure 9**, comparing the as-printed 316LMn, as-printed Nitronic-50, and annealed Nitronic-50. Tests were also conducted along the bead direction, build direction, and 45-degree from both directions. For almost all materials in the present study, the 45-degree specimens showed the highest yield strength (YS) and ultimate tensile strength (UTS) among three different tensile axes, and the total plastic elongation (EL) and the reduction of area (RoA) exhibited an opposite trend. It should also be emphasized that the YS and UTS along the build direction was always higher than those along the bead direction, and the opposite trends appeared on EL and RoA, suggesting that the crystallographic anisotropy might account for the differences in the tensile properties. The trends were observed at both RT and -196°C. The as-printed Nitronic-50 also showed higher YS and UTS and lower EL and RoA than those of the annealed sample, which might reflect the effect of δ-ferrite on increasing deformation resistance and losing ductility. Since the as-printed 316LMn and the annealed Nitronic-50 showed similar tensile properties, δ-ferrite is considered as one of the strong factors to control the mechanical properties.

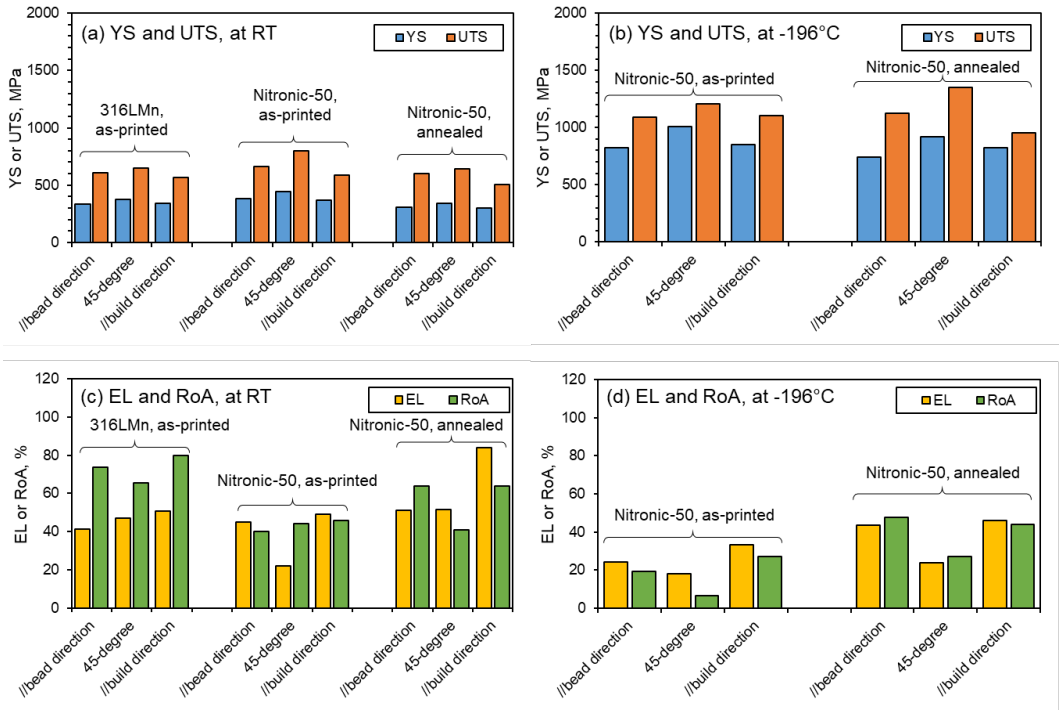

Figure 9. Tensile test results of the as-printed 316LMn, as-printed Nitronic-50, and annealed Nitronic-50, showing YS and UTS at RT (a) and at -196°C (b), and EL and RoA at RT (c) and at -196°C (d).

The tensile data comparing with the properties of commercial products, 316LMn weld and an annealed Nitronic-50 [3,4], are summarized in **Table 2** and **Table 3**.
The present results indicated that most of the YS, UTS, and RoA were lower than the commercial weld or wrought products, whereas the EL exceeded the reference data. When focusing on the ductility, the as-printed Nitronic-50 was significantly lower than the others as well as the commercial wrought products.

Table 2. Summary of tensile properties at room temperature

Specimen	Tensile axis	YS, MPa	UTS, Mpa	EL, %	RoA, %	Remarks
316LMn, as-printed	//bead direction	337 ± 15	609 ± 6	41 ± 4	74 ± 7	averaged 3 test results
	45-degree	374 ± 8	647 ± 16	47 ± 4	65 ± 5	
	//build direction	339 ± 3	567 ± 14	51 ± 5	80 ± 6	
ER316LMn	n.a.	434	690	>30	-	Weld metal [ref. 2]
Nitronic-50, as-printed	//bead direction	383	662	45	40	1 test only
	45-degree	441	800	22	44	
	//build direction	369	586	49	46	
Nitronic-50, annealed	//bead direction	309	603	51	64	1 test only
	45-degree	338	641	52	41	
	//build direction	301	503	84	64	
Nitronic-50, datasheet	n.a.	415	690	35	55	Annealed condition [ref. 3]

Table 3. Summary of tensile properties of Nitronic-50 at -196°C

Specimen	Tensile axis	YS, MPa	UTS, Mpa	EL, %	RoA, %	Remarks
Nitronic-50, as-printed	//bead direction	826 ± 12	1088 ± 9	24 ± 3	20 ± 3	averaged 3 test results
	45-degree	1009 ± 22	1208 ± 63	18 ± 8	7 ± 2	
	//build direction	853 ± 9	1105 ± 73	33 ± 4	27 ± 2	
Nitronic-50, annealed	//bead direction	741 ± 9	1124 ± 12	44 ± 10	48 ± 2	averaged 3 test results
	45-degree	918 ± 14	1353 ± 23	24 ± 3	27 ± 5	
	//build direction	823 ± 11	954 ± 47	46 ± 11	44 ± 10	
Nitronic-50, datasheet	n.a.	883	1558	41	51	Annealed condition [ref. 3]

3.3.2 Charpy impact toughness

Figure 10 shows the Charpy impact absorbed energy of the as-printed 316LMn and the annealed Nitronic-50 plotted as a function of test temperature, from RT to -196°C. Tests were conducted with three different specimen orientations as illustrated in the plot (note: the crack propagation is always parallel to the wall thickness direction or X-axis). Both materials showed quite similar test results with relatively small variation among the specimen orientations. The small variation was possibly attributed to similar alloy compositions and microstructures, although a small amount of the residual δ-ferrite observed in the annealed Nitronic-50 might absorb less energy than that of the as-printed 316LMn. The absorbed energy of commercial wrought Nitronic-50 [4] is 68 J at -196°C, so the shown results of both materials at -196°C was comparable to the reference data.

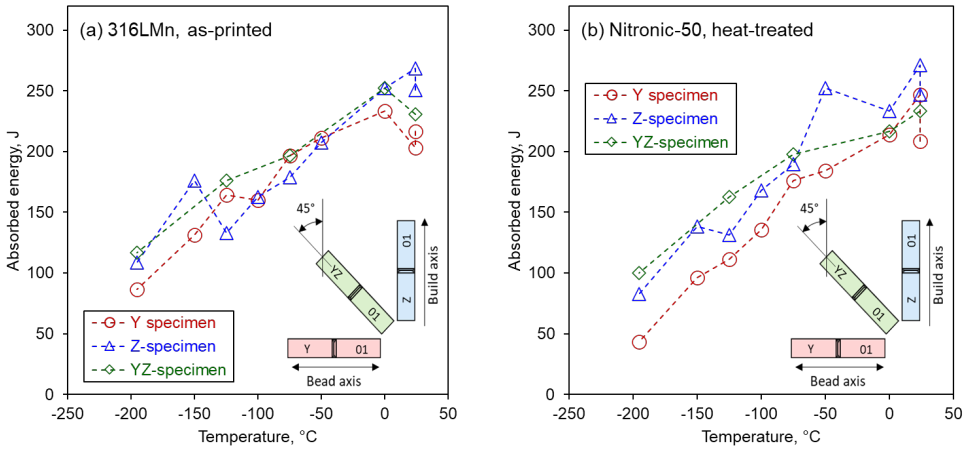

Figure 10. Charpy absorbed energy plotted as a function of test temperature: (a) 316LMn, as-printed, and (b) Nitronic-50, annealed.

3.3.3 Fracture toughness

The 0.5-inch thick (0.5T) compact tension (CT) specimens were machined from the annealed Nitronic-50 wall. A total of six specimens were machined with specimen IDs YZ-1 through YZ-3 and ZY-1 through ZY-3. The detailed drawing of the 0.5T CT specimen can be seen in **Figure 11**. The tests were conducted only on YZ-1, YZ-2, ZY-1, and ZY-2, and the rest of the specimens were kept as spares.

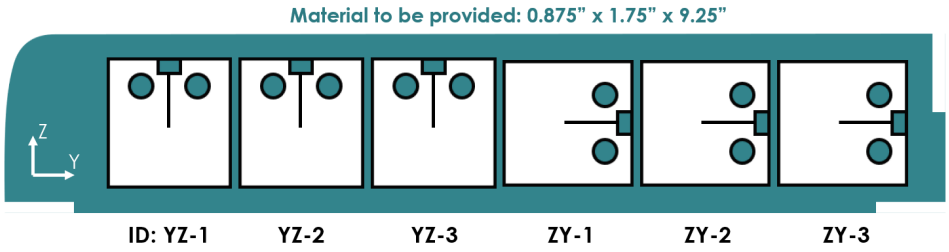

Figure 11. Schematic of machined fracture toughness specimens

The J-R curve results of the test specimens are shown in **Figure 12** with the summary results listed in **Table 4**. Overall, all specimens showed relatively high initiation fracture toughness, JIC, with ZY-series specimens showing higher JIC than YZ-series specimens on average. While the YZ-series specimens may appear to have higher tearing modulus, a measure of material's resistance against further crack growth, than ZY-series specimens, it is worth noting that YZ-series specimens exhibited unstable cleavage-like fracture after limited ductile crack growth therefore the concept of tearing modulus may not apply for the specimens.

Table 4. Summary of fracture toughness characterization

Specimen ID	Test temperature (°C)	J_{IC} (kJ/m^2)	Tearing modulus	Note
YZ-1	-192.5	214.1	91.4	Limited ductile crack growth followed by cleavage-like fracture
YZ-2	-193.1	247.8	60.8	
ZY-1	-195.4	356.2	51.3	Ductile crack growth
ZY-2	-193.5	246.8	53.9	

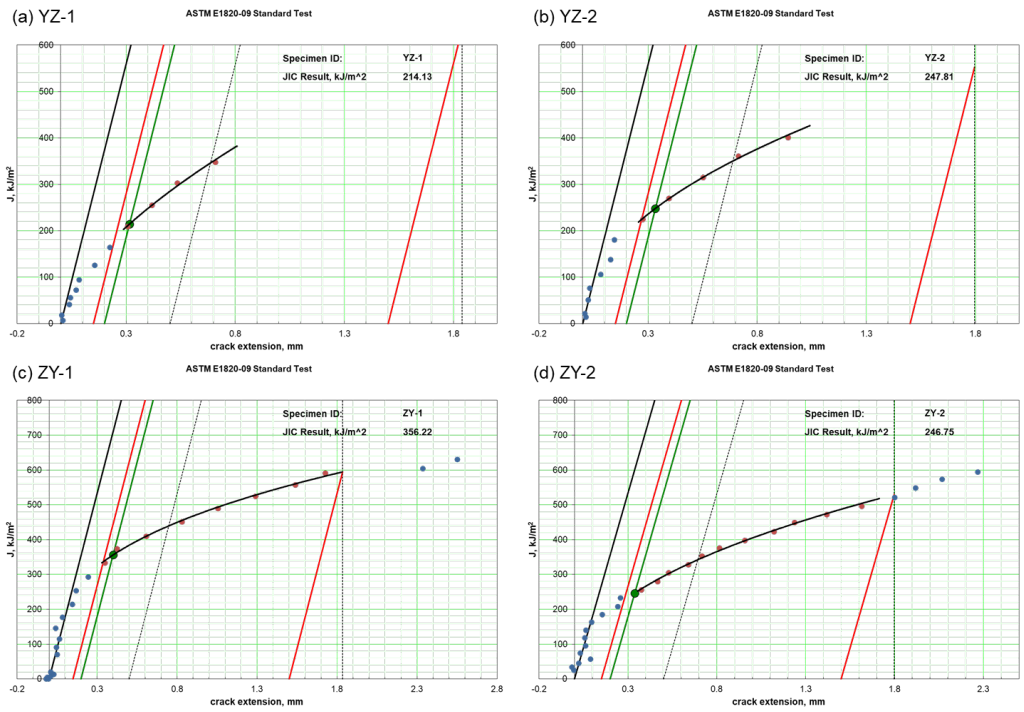

Figure 12. J-R curves of (a) YZ-1, (b) YZ-2, (c) ZY-1, and (d) ZY-2

4. DEMO PRINT

4.1 TRIAL DEMO COMPONENT PRODUCTION

For the final test, a toroidal shield device was selected. 316LMn feedstock was chose for manufacturing of this part.
In order to take advantage of additive manufacturing and the unique characteristic of the geometry the process printing process was modified. The standard approach for AM selects a fixed z-axis for printing,

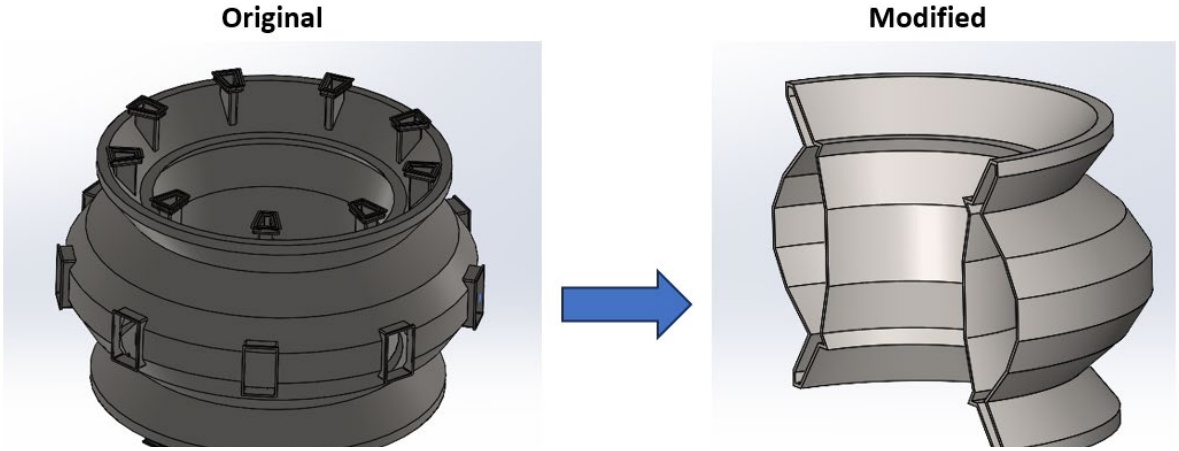

Figure 13. Vacuum vessel model (left) and simplified geometry (right)

effectively following what is called crating (2.5D printing where the layers are flat and aligned in the direction of the z-axis). For this part, a new approach was taken, which follows a circumferential direction of print (where the "z-axis" is curved to follow the part) and required varying bead geometry.

4.1.1 Process modification and controls

The objective was to determine if a 3-dimensional layer profile for a single layer is possible by alternating the bead geometry. This is different from a 2.5D layer profile, as 2.5D printing uses the same layer-height bead geometry for the entire layer. Constant bead geometries have difficulties when conforming to non-planar surfaces, as a constant bead with regular spacing will have difficulty filling an irregular volume (in this case, square cross-section beads filling a wedge-shaped part cross-section). This results in separation of the bead paths and introduces discontinuous bead segments to fill up the gaps. These bead segments slow down the printing process and potentially lead to voids due to the breaks. By using a 3D bead profile, the full cross-sectional area can be filled by modifying the bead geometry in-process, thereby mitigating bead path segmentation.

To understand the effects of process controls on bead geometry, multiple single-bead thick walls were printed out of 316LMn. Both robot travel speed and wire feed speed were varied. Travel speed ranged from 20 to 60 in/min in increments of 10 in/min, and the wire feed speed ranged from 300 to 500 in/min in increments of 50 in/min. This gave a total of five discrete travel speeds and wire feed speeds, which resulted in printing 25 walls. Each wall was 10" long and 50 layers tall. Both the bead width and average layer height were obtained. Arc stability for each change was noted to understand the limits when varying these two inputs. The first wall printed used a stable weld process and served as the baseline. The baseline process parameters used are presented in Table 5.

Table 5. Baseline process parameters

Shielding gas	98% Ar, 2% CO_2
Weave length (mm)	3
Weave width (mm)	0.2
Weld mode	284 (Rapid X)
Trim	1.05
Travel Speed (in/min)	40
Wire feed speed (in/min)	400
Voltage (V)	25.3
Current (A)	245

The resulting comparison graphs are shown in Figure 14 and Figure 15.

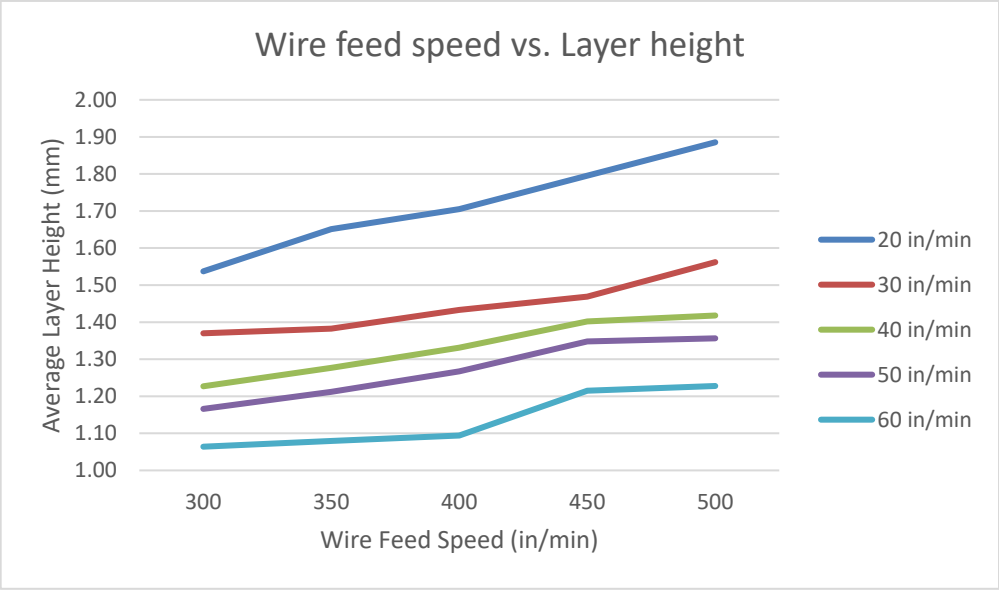

Figure 14. Average layer height as a function of wire feed and print head speed

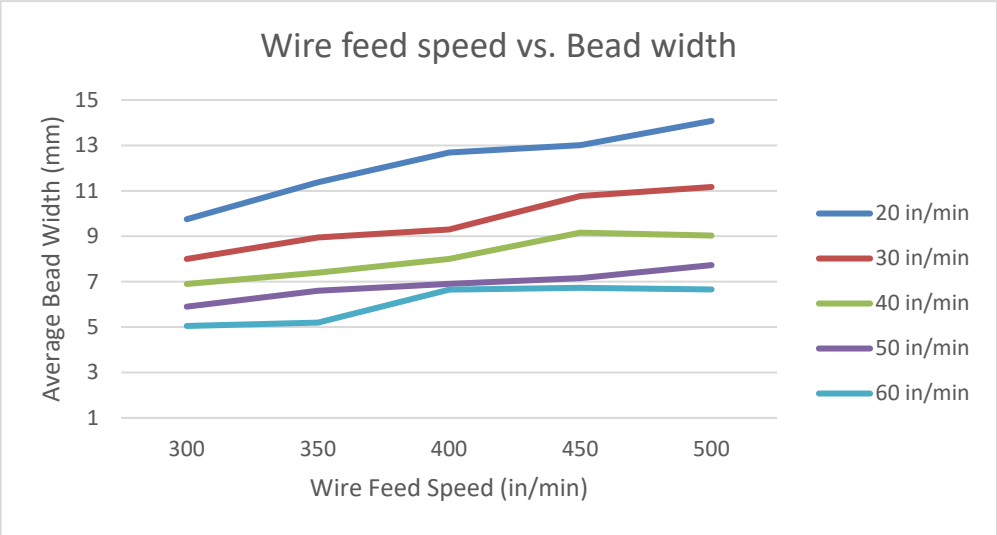

Figure 15. Average bead width as a function of wire feed speed and print head speed

The results showed that decreasing the travel speed while increasing the wire feed speed increases both the height and width of a single printed bead. Using a combination of both the wire feed speed and travel speed allowed for larger changes in layer height. The correlation is also mostly linear. Unstable weld processes occurred when using a travel speed of 60 in/min and a wire feed speed of and above 350 in/min.

4.2 SIMPLIFIED TOROID GEOMETRY

The original geometry provided by CFS was simplified to a rectangular cross-section for testing purposes. A two-axis positioner was used as the main method to create the revolved geometry. A custom program was developed to properly transform the layer profile based on the angle of the positioner (i.e., splitting the part into layer "wedges"). Using the baseline parameters, a centerline layer height of 1.33 mm was obtained. This layer height was then used for the center of the cross-section. This can be seen in **Figure 16**. Additionally, the arc length was used to calculate the number of layers. With an obtained arc length of 967.61 mm, the total layer count was 728 layers. The part had a revolved extrusion of 180°. Dividing this with the total layer count, the degrees per layer can be obtained, which was 0.247°. The degrees per layer was used as the value to incrementally rotate the positioner every layer. Since the center point of the revolved geometry is located at the axis of rotation of the positioner, the toolpath generated from the slicer had additional information that specify wire feed speed and travel speed based on radial location. This experiment was conducted to test the feasibility of using this method.

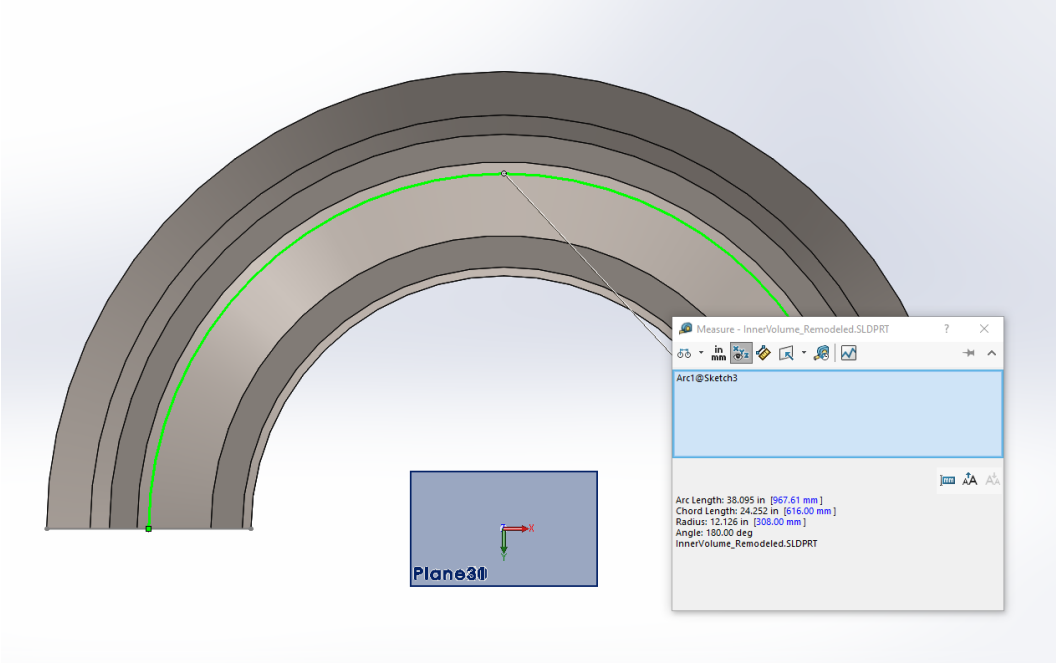

Figure 16. Acquired arc length for the center of the cross-section.

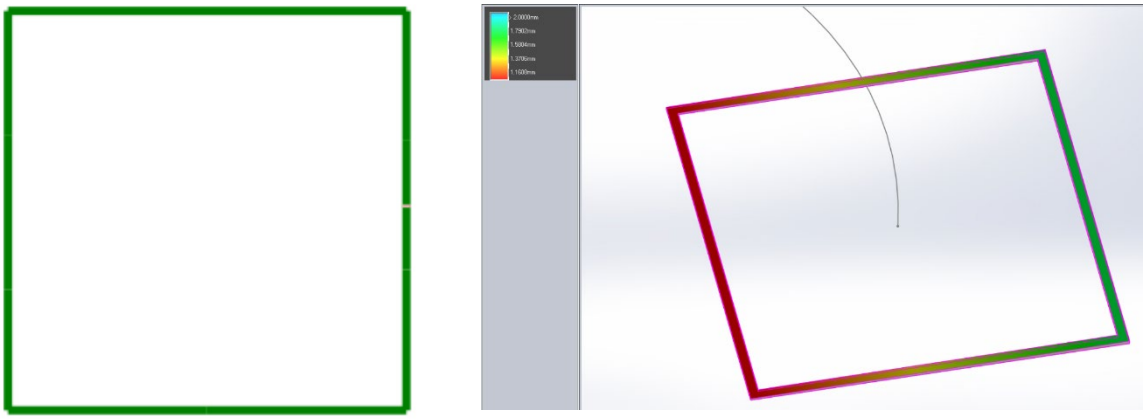

Figure 17. Resulting bead shape (left) and required changes in layer height based on radial profile (right).

The outcome of this experiment was a printed toroidal part. The adaptive height control assisted in maintaining the proper layer heights for the print. When comparing the scan (**Figure 18**) with the CAD model, the typical deviation was 1.06 mm (**Figure 19**). The final test part is presented in **Figure 20**.

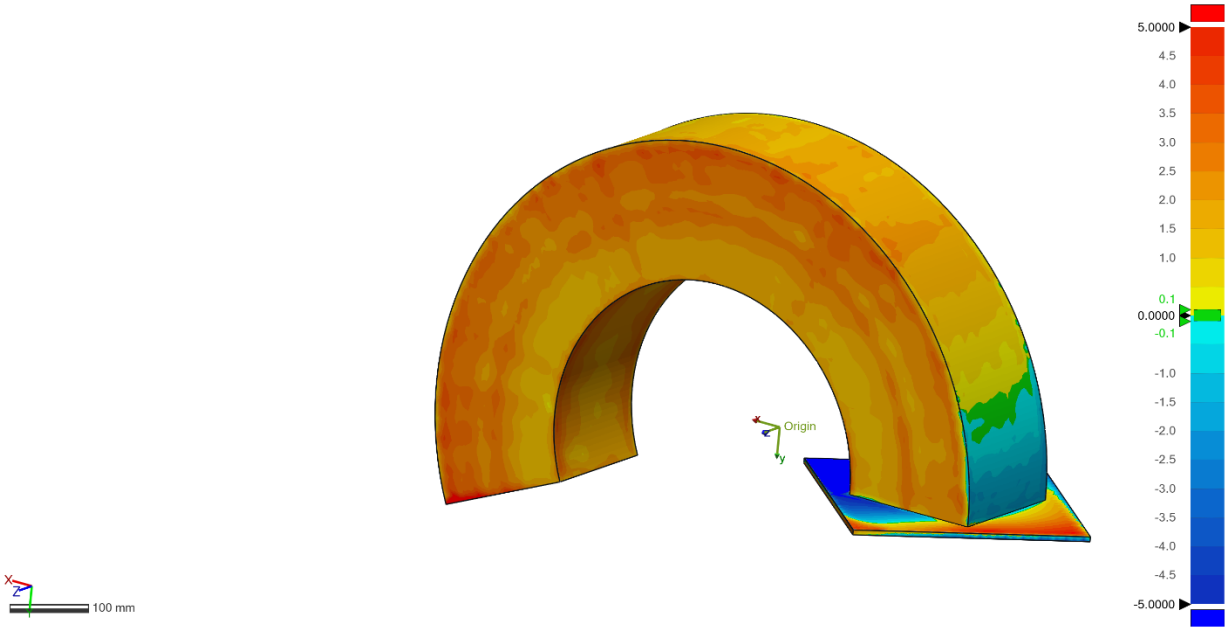

Figure 18. Scanned toroidal test component. Color representing deviation from the model.

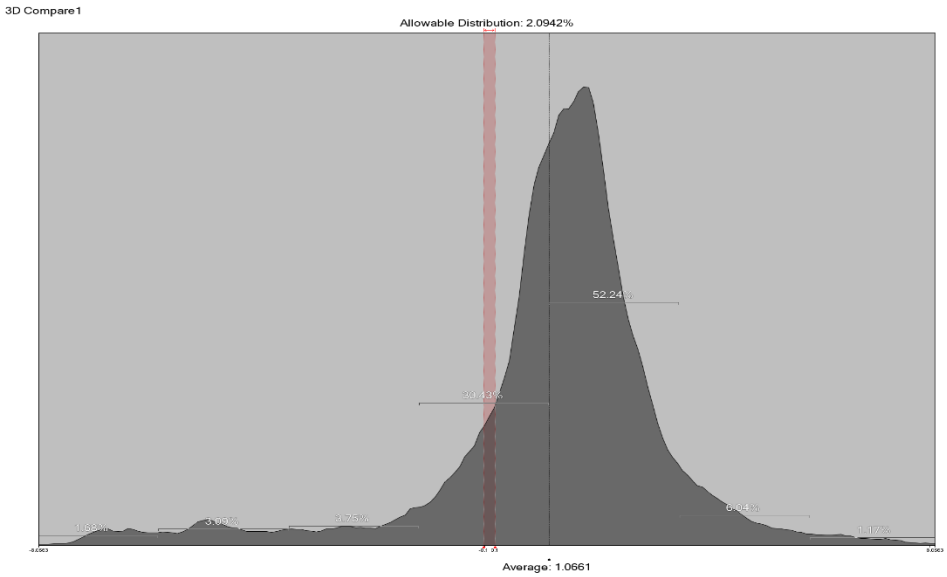

Figure 19. Print geometry error distribution.

Figure 20. Test part during the print (left) and the finished part (right).

4.2.1 Property screening

To evaluate the mechanical properties and microstructure of the as printed 316LMn test component, an additional part with the print condition same as the large demonstration component was printed, as shown in **Figure 21**.

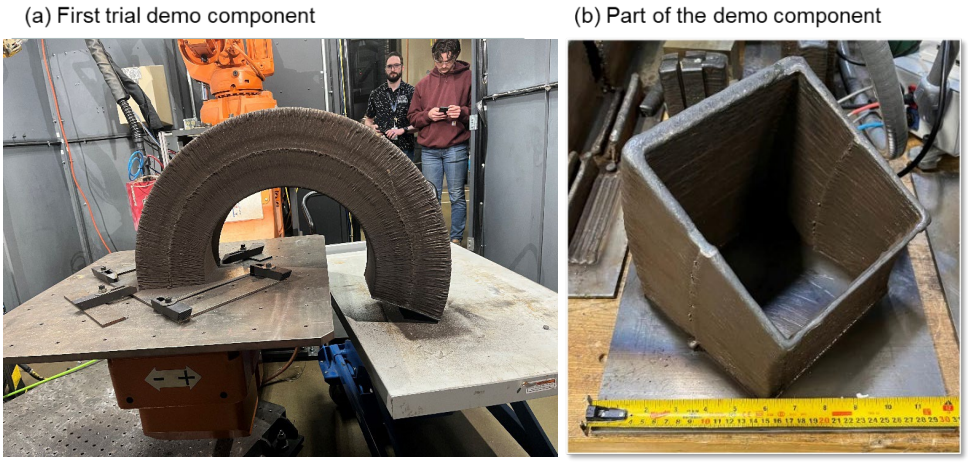

Figure 21. First trial demonstration component made of 316LMn (a) and additionally printed part for property screening (b)

The additionally printed part was sectioned into four walls, and multiple tensile specimens as well as metallographic specimens were machined with different orientations at each wall, as illustrated in **Figure 22**. Total four of metallographic specimens, eight of ASTM -E8 dog-bone shape tensile specimens, and three of sub-sized tensile specimens (SS-3) were tested at room temperature.

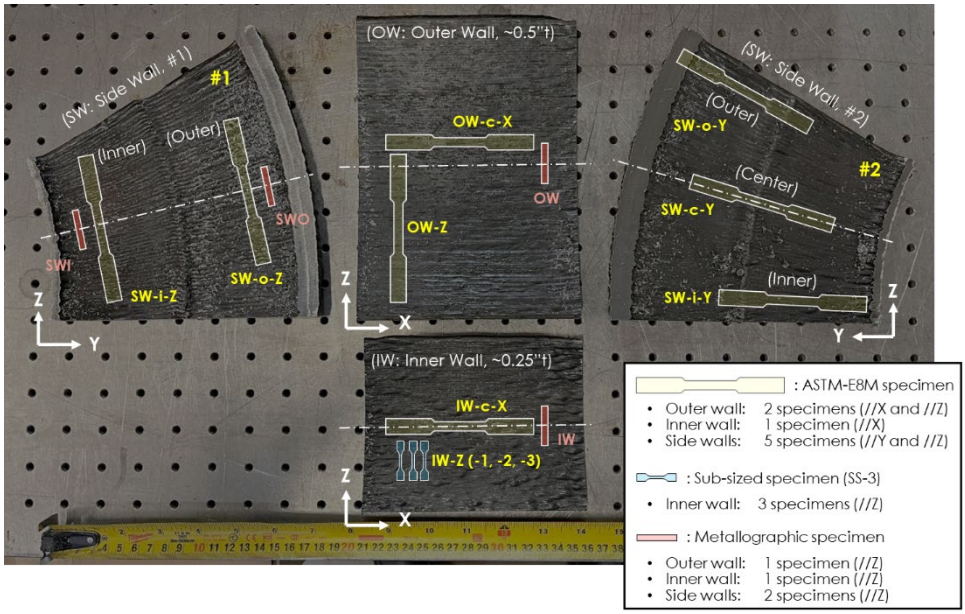

Figure 22. Sectioning plan of tensile specimens and metallographic specimens from the as-printed 316LMn demo component

Microstructure characterization revealed that similar bead structures were observed with almost no defect formation. Some pores were also observed on the side wall, as indicated by yellow arrows in **Figure 23**, although they are considered minor defects and can be eliminated by further optimization of the print conditions. The thickness of layers decreased from the outer wall to the inner wall, from left to right in **Figure 23**, which represented the design of continuous layer thickness change (wedge-shaped layers) for the overall toroidal-shaped component production.

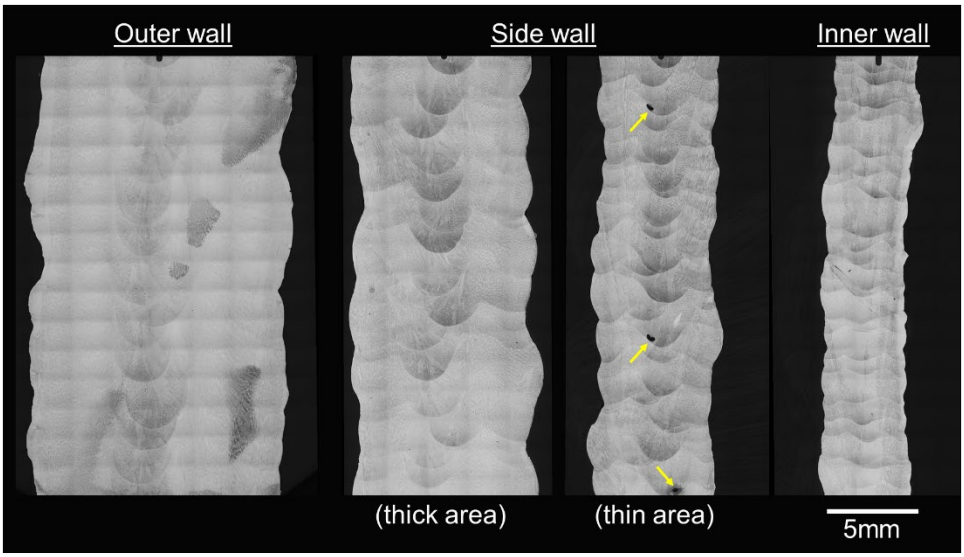

Figure 23. Cross-sectional macrostructure of the as-printed 316LMn demo component

The obtained tensile properties are summarized in **Table 6**. There was a tendency for the inner wall strengths to be larger than the outer wall, and an opposite trend in the ductility. The trend could be attributed to finer microstructure in the inner wall than that of the outer wall, although the variations of the strengths and ductility among the different locations and direction were relatively small (YS: ± 6%, UTS: ± 6%, EL: ± 16%, RoA: ± 18%) and therefore the property inhomogeneity in the demo component is considered not significant.

Table 6. Summary of tensile properties of the as-printed 316LMn demo part at room temperature

Direction	Test orientation	Part	Position	**Specimen ID**	YS, MPa	UTS, MPa	Uniform EL, %	Total EL, %	Modulus, GPa	Specimen
Along the beads	X-axis	Outer wall	Near center	**OW-C-X**	312	579	42.0	52.0	118.2	ASTM-E8
		Inner wall	Near center	**IW-C-X**	337	601	33.0	39.7	142.0	
	Y-axis	Side wall	Near outer	**SW-O-Y**	309	590	34.9	41.2	143.4	
			Near center	**SW-C-Y**	330	597	37.1	45.0	121.6	
			Near inner	**SW-I-Y**	316	593	39.5	46.9	131.1	
Across the beads	Z-axis	Outer wall	Near center	**OW-Z**	302	547	46.0	57.0	120.3	ASTM-E8
		Inner wall	Near center	**IWZ-1**	323	545	43.9	53.6	N.A.	SS-3
				IWZ-2	333	542	38.7	41.6	N.A.	
				IWZ-3	325	568	41.1	44.9	N.A.	
		Side wall	Near outer	**SW-O-Z**	305	537	45.5	54.1	159.0	ASTM-E8
			Near inner	**SW-I-Z**	323	557	43.9	52.1	146.1	

4.3 MINIATURE 3D COMPONENT PRODUCTION

The original vessel model was scaled down and defeatured for the part to fit and be printable for an additive manufacturing system (**Figure 24**). The toroidal shape was kept, as this was the critical geometry of the design. The toolpath was created based on a constant model cross section however (**Figure 25**), depending on the distance to the center of rotation, bead sections were tagged to have varying height and width. The square profile test geometry method was used as a model to evaluate the validity of the varying bead process parameters and their combined successful effect in producing non-planar layers. A total of 10 different combinations of wire feed speed and travel speed were used. The completed part is presented in **Figure 26**. In the last step, the printed part was 3D scanned and compared with the CAD model. A comparison between the scan and the model resulted in an average 0.85 mm deviation (**Figure 28**). The weight of the part was approximately 150lsb with inner radius of 8.6", outer radius 15.6" and the cross-section bounding box of 19x7". The final part was delivered to CFS.

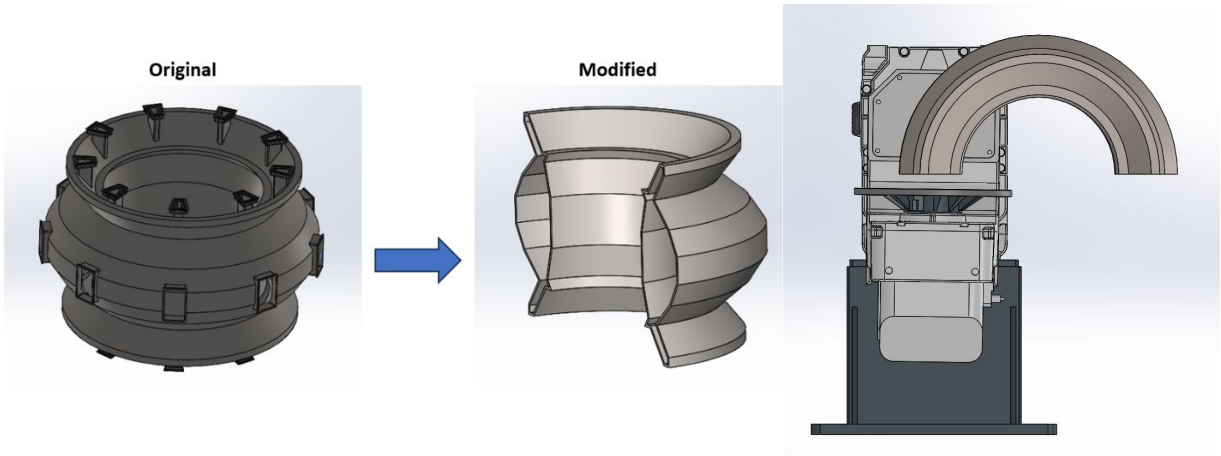

Figure 24 Model of the shield (left), defeatured part (middle), modeled part on the positioner.

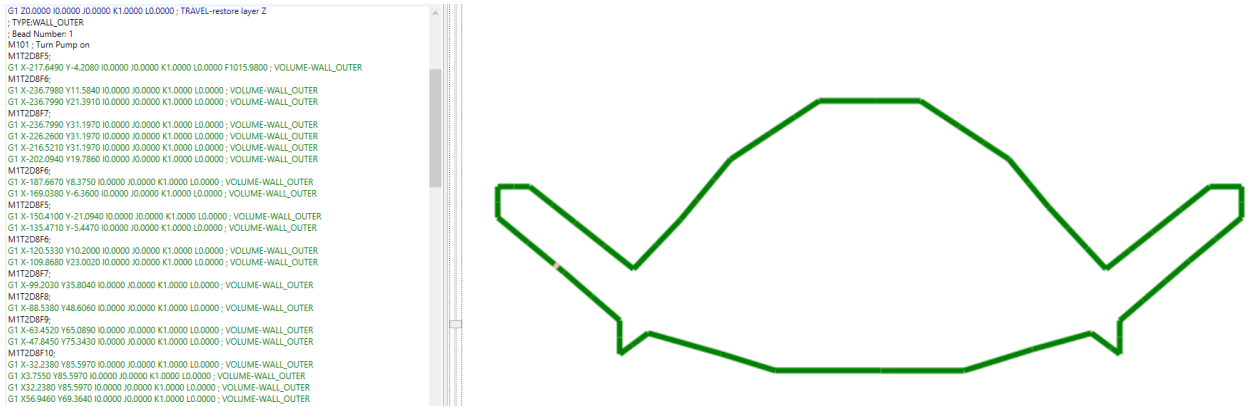

Figure 25.ORNL slicer Toolpath (left) and part cross section bead model (right).

Figure 26. Final part during manufacturing (left) and finished part (right).

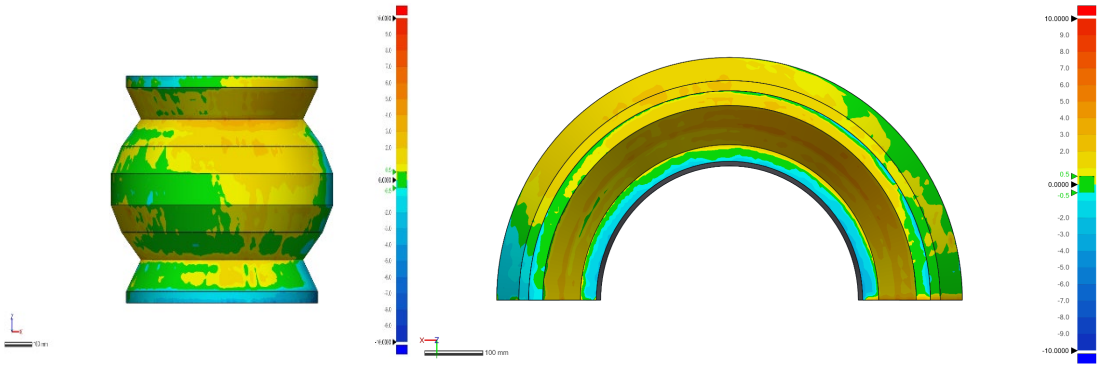

Figure 27. Heatmap comparison of the printed part and the model (not to scale).

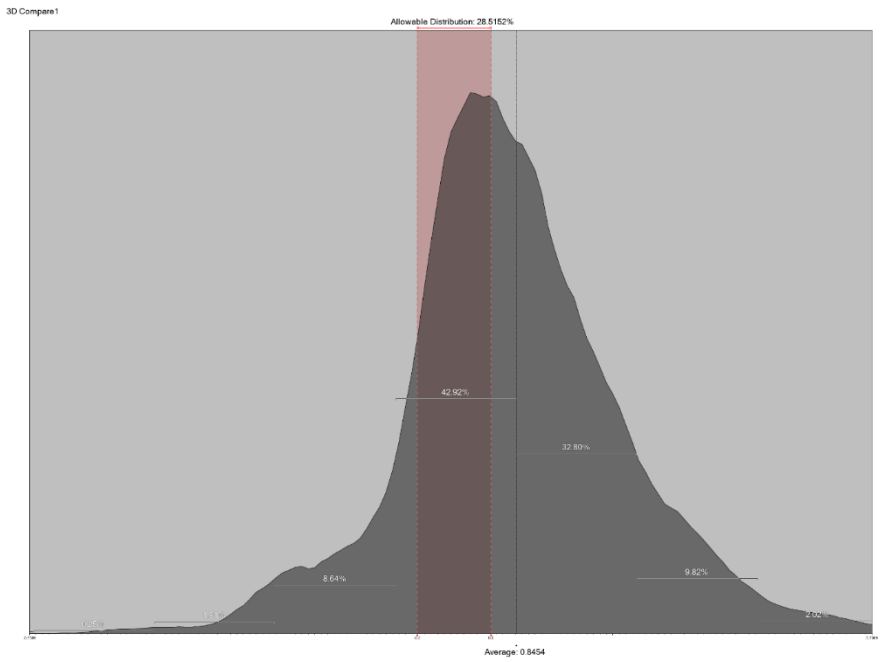

Figure 28 Final print geometry error distribution

5. USE OF PROJECT RESULTS

Results of this project will be used by Commonwealth Fusion Systems to inform the materials and manufacturing R&D roadmap being used to bridge the gap in available technologies to deliver a fusion power plant. While the grades of austenitic stainless steel used for development prints in this project are unlikely to be used for the primary integrated vacuum vessel for the ARC fusion power plant, the print optimization steps (geometry, wire speed matrix, etc.) all provide useful background to future manufacturing planning once prime candidate material is selected for the ARC vessel. Other components of the ARC plant may require materials in these grades, and, if so, the proof of demonstration material property sets demonstrated here will be used as for initial engineering analysis.

6. INTELLECTUAL PROPERTY, PUBLICATIONS, AND CONFERENCES

No intellectual property was generated during the course of this project. A conference presentation highlighting this work have been given at the FY2023 INFUSE Workshop on October 19 in conjunction with the 64th Annual Meeting of the APS Division of Plasma Physics (DPP).

7. FUSION ENERGY IMPACT & CONCLUSIONS

During this project, a new way of manufacturing fusion device components was successfully demonstrated using wire-arc additive technology. A workflow for designing and testing non-uniform layered printing was developed along with manufacturing two demonstration components. Furthermore, a process creating specific toroidal parts was developed and tested. Two different materials were studied, stainless steel 316LMn and Nitronic 50, their process parameters were developed, and mechanical properties were obtained. The selected technology (wire-arc) is very scalable and gaining fast adoption in

the metal manufacturing industry. The full adoption of a fusion energy ecosystem will require the use of rapid and flexible manufacturing methods such as those demonstrated here to meet the capacity factors necessary for economic power generation.

8. ACKNOWLEDGEMENTS

The wire-arc technology used to manufacture the components was developed in collaboration with Lincoln Electric under a Cooperative Research and Development Agreement.

9. REFERENCES

1. Nycz, Andrzej, Adeola I. Adediran, Mark W. Noakes, and Lonnie J. Love. "Large scale metal additive techniques review." In *2016 International Solid Freeform Fabrication Symposium*. University of Texas at Austin, 2016
2. Saket Thapliyal, Jiahao Cheng, Jason Mayeur, Yukinori Yamamoto, Patxi Fernandez-Zelaia, Andrzej Nycz & Michael M. Kirka, "Outlook on texture evolution in additively manufactured stainless steels: Prospect1s for hydrogen embrittlement resistance, overview of mechanical, and solidification behavior", Journal of Materials Research (2023). https://doi.org/10.1557/s43578-023-01130-6
3. Midlloy Technical Bulletin, "Midalloy ER 316LMn Bare Wire", https://www.midalloy.com/wp-content/uploads/2016/08/TB-ER316LMn-Bare-Wire.pdf (as of 9/7/2023)
4. AK Steel International product data bulletin, "ARMO Nitronic 50", https://www.aksteel.nl/files/downloads/ak_steel_armco%C2%AE_nitronic%C2%AE_50_product_data_bulletin_-jan__2019-_94.pdf (as of 9/7/2023)